Hierarchically Structured Microfibers of 'Single Stack' Perylene Bisimide and Quaterthiophene Nanowires

Supporting Information

Roman Marty,[1] Ruth Szilluweit,[1] Antoni Sánchez-Ferrer,[2] Sreenath Bolisetty,[2]

Jozef Adamcik,[2] Raffaele Mezzenga,[2] Eike-Christian Spitzner,[3] Martin Feifer,[3]

Stephan N. Steinmann,[4] Clémence Corminboeuf,[4] and Holger Frauenrath[1,]*

[1] Ecole Polytechnique Fédérale de Lausanne (EPFL), Switzerland
Institute of Materials
Laboratory of Macromolecular and Organic Materials

EPFL – STI – IMX – LMOM, MXG 037, Station 12
1015 Lausanne, Switzerland

holger.frauenrath@epfl.ch

[2] ETH Zürich, Switzerland
Department of Health Sciences and Technology

[3] Technische Universität Chemnitz
Fakultät für Naturwissenschaften
09126 Chemnitz, Germany

[4] Ecole Polytechnique Fédérale de Lausanne (EPFL), Switzerland
Institute of Chemical Sciences and Engineering
Laboratory for Computational Molecular Design

Table of Contents

1. Supplementary Figures S1–S19

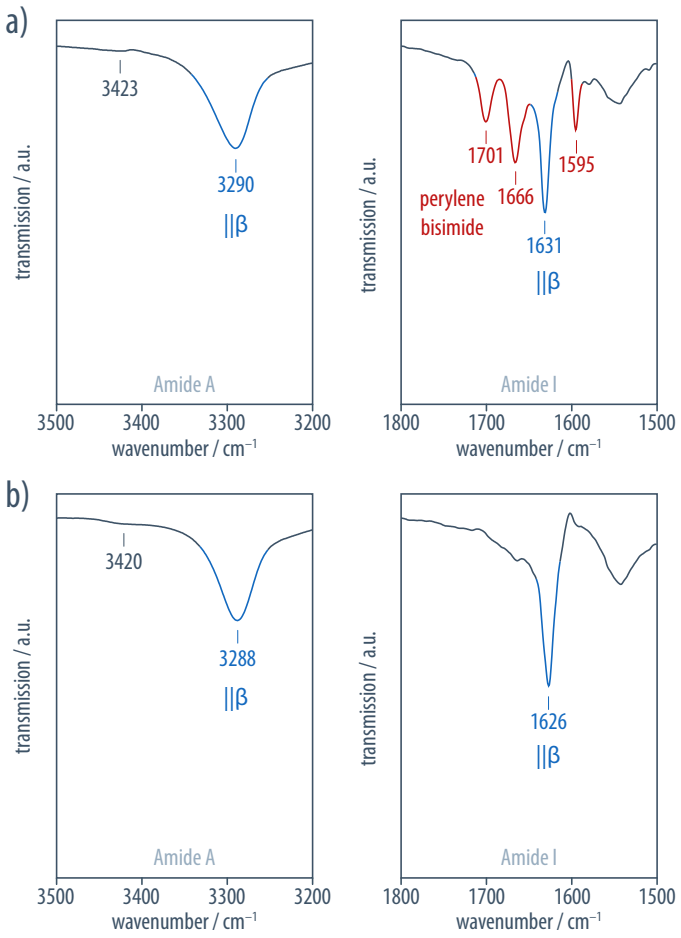

Supplementary Figure S1. Solution-phase IR spectra of thermally annealed solutions of *a)* perylene bisimide **1**, and *b)* quaterthiophene **2** in 1,1,2,2-tetrachloroethane (TCE; $c = 1 \cdot 10^{-3}$ mol/L) showed a single amide A (ν_{N-H}) absorption band at around 3290 cm^{-1}, a sharp amide I ($\nu_{C=O}$) band at around 1630 cm^{-1} (both blue), as well as the absence of the secondary amide I component at 1695 cm^{-1}, all of which is consistent with the formation of well-ordered parallel β-sheet-type aggregates in TCE solution. The weak additional amide A bands at about 3420 cm^{-1} indicated small amounts of residual non-aggregated molecules. The absorption bands at 1701 cm^{-1}, 1666 cm^{-1}, and 1595 cm^{-1} in the spectrum of **1** (red) are associated with carbonyl and benzene vibrations of the perylene bisimide core.

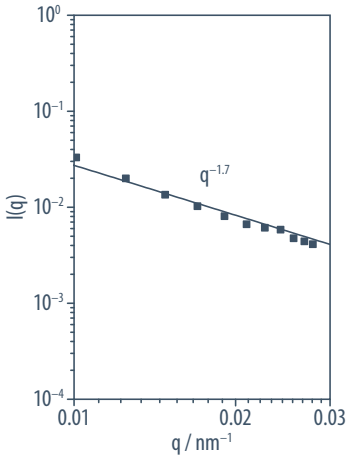

Supplementary Figure S2. Linear fitting of the static light scattering intensities $I(q)$ of a solution of **2** (TCE; $c = 1 \cdot 10^{-4}$ mol/L) versus the scattering vector (q) resulted in the solid line with a slope of -1.7 (≈5/3), confirming the presence of semiflexible fibrillar structures with excluded volume interactions.

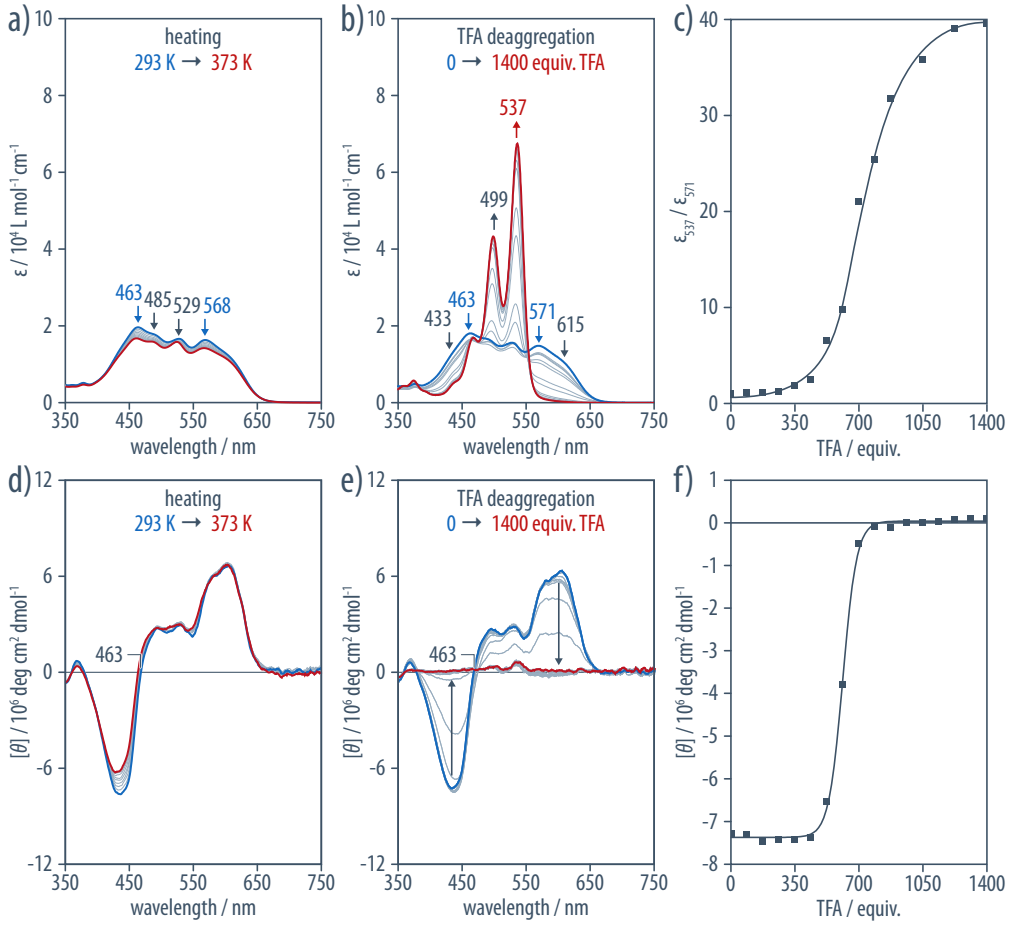

Supplementary Figure S3. *a)* UV/vis spectroscopy of a thermally annealed solution of **1** (TCE; $c = 1 \cdot 10^{-3}$ mol/L, blue curve) revealed that the global absorption maximum at 463 nm was significantly blue-shifted as compared to the one of molecularly dissolved perylene bisimide derivatives, which is usually observed at around 525 nm. This hypsochromic shift combined with the appearance of a bathochromically shifted absorption band at 569 nm and a shoulder at 615 nm suggested the presence of strongly cofacially aggregated but rotationally displaced perylene bisimide cores.[1] The aggregates were stable up to 373 K (red curve), which was the heating limit of the Peltier element. *b)* Titration of the solution (blue curve) with a significant excess of trifluoroacetic acid (TFA) as a hydrogen-bond-breaking agent furnished solutions of **1** showing the typical fine structure of molecularly dispersed perylene bisimides (red curve), with a global maximum at 537 nm (exhibiting a small solvatochromic effect due to the addition of TFA). The samples for the titration series were prepared by adding up to 8 µL (1400 equiv.) of TFA in steps 0.5 µL to separate vials containing 750 µL of a $1 \cdot 10^{-4}$ mol/L TCE-solution. *c)* A plot of the relative intensities of the absorptions at 537 and 571 nm versus the amount of TFA showed that the addition of TFA resulted in complete deaggregation. *d)* CD-spectroscopy of a solution of **1** (TCE; $c = 1 \cdot 10^{-4}$ mol/L, blue curve) revealed strong bisignate CD bands with a negative maximum at 433 nm, a zero-crossing at 461 nm (corresponding to the maximum UV/vis absorption), and a positive maximum at 605 nm, indicating a positive Cotton effect and, thus, the presence of π–π stacked perylene bisimide chromophores in a *P*-helical arrangement that remained stable upon heating to 373 K (red curve).[2,3] *e)* Upon the addition of TFA, the solutions of **1** (blue curve) became CD-inactive (red curve). *f)* Consistent with UV/vis spectroscopy, a plot of the molar ellipticity at 433 nm versus the amount of TFA indicated that the aggregates were disassembled upon TFA addition. In all of the displayed UV/vis and CD spectral series, the grey curves represent the intermediate spectra obtained by increasing the temperature in steps of 10 K from 303 to 363 K, or by increasing the amount of TFA in steps of 88 equivalents from 88 to 1312 equivalents, respectively.

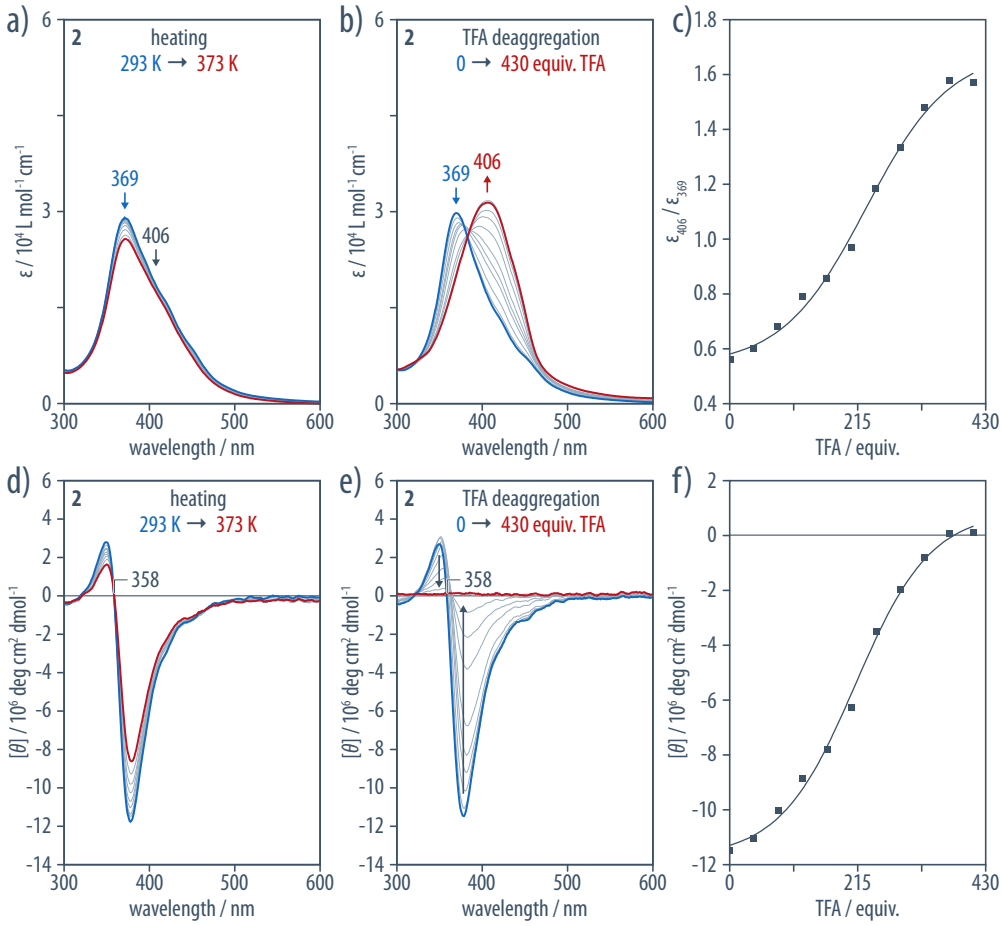

Supplementary Figure S4. *a)* UV/vis spectroscopy of a thermally annealed solution of **2** (TCE; $c = 1 \cdot 10^{-3}$ mol/L, blue curve) revealed that the global absorption maximum at 369 nm was significantly blue-shifted as compared to the one of molecularly dissolved quaterthiophene derivatives, which is usually observed at around 406 nm. The aggregates were stable up to 373 K (red curve), which was the heating limit of the Peltier element. *b)* Titration of the solution (blue curve) with a significant excess of trifluoroacetic acid (TFA) as a hydrogen-bond-breaking agent furnished solutions of **2** with a global maximum at 406 nm characteristic for molecularly disperse quaterthiophene solutions (red curve). The samples for the titration series were prepared by adding up to 3.33 µL (430 equiv.) of TFA in steps of 0.33 µL to separate vials containing 1 mL of a $1 \cdot 10^{-4}$ mol/L TCE-solution. *c)* A plot of the relative intensities of the absorptions at 406 and 369 nm versus the amount of TFA showed that the TFA addition induced significant deaggregation. *d)* CD-spectroscopy of a solution of **2** (TCE; $c = 1 \cdot 10^{-4}$ mol/L, blue curve) revealed strong bisignate CD bands with a negative maximum at 377 nm, a zero-crossing at 358 nm, and a positive maximum at 348 nm, indicating a negative Cotton effect and, thus, the presence of π–π stacked quaterthiophene chromophores in a *M*-helical arrangement that remained relatively stable upon heating to 373 K (red curve).[4] *e)* Upon the addition of TFA, the solutions of **2** (blue curve) became CD-inactive (red curve), proving that the molecular chirality of **2** was not the origin of the observed CD activity of the aggregated species. *f)* Consistent with UV/vis spectroscopy, a plot of the molar ellipticity at 377 nm versus the amount of TFA (red curve) indicated that the aggregates were disassembled upon TFA addition. In all of the displayed UV/vis and CD spectral series, the grey curves represent the intermediate spectra obtained by increasing the temperature in steps of 10 K from 303 to 363 K, or by increasing the amount of TFA in steps of 43 equivalents from 43 to 387 equivalents, respectively.

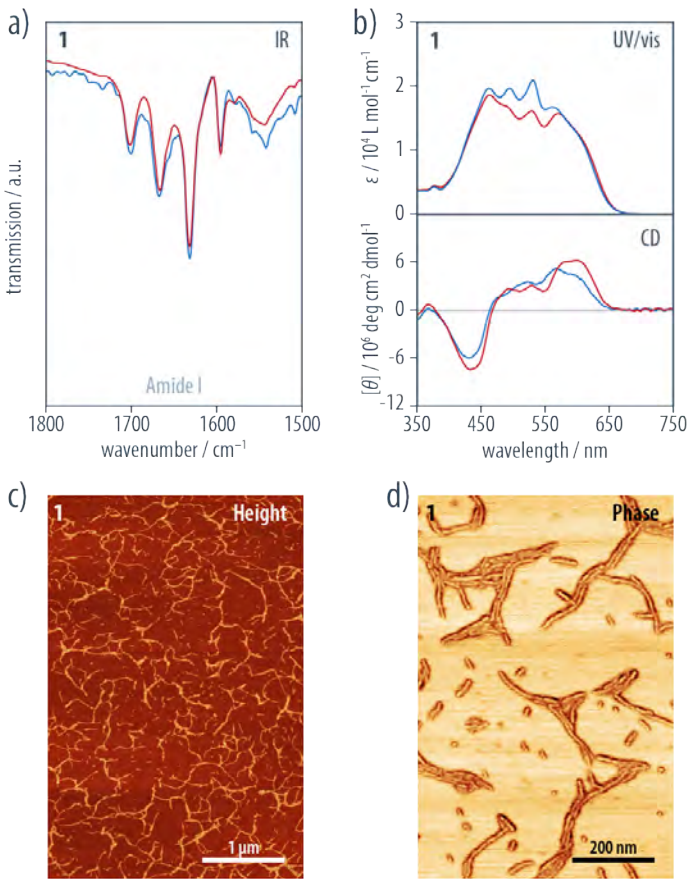

Supplementary Figure S5. *a)* IR spectra of a solution of **1** (TCE; $c = 1 \cdot 10^{-3}$ mol/L) and *b)* the solution-phase UV/vis and CD spectra (TCE; $c = 1 \cdot 10^{-4}$ mol/L) as obtained after dissolution of the material (blue curves) showed marginal differences when compared to a thermally annealed solution (red curves). The main IR absorptions were located at the same wavenumber and showed comparable intensities for both samples. While the UV/vis spectra of both solutions indicated the presence of strongly π–π stacked chromophores in a helical environment, thermal annealing resulted in a decrease of the intensity of the absorption band at around 531 nm and an increase of the absorption intensity at around 463 nm. The molar ellipticities at the maxima and minima in the CD spectra slightly increased upon thermal annealing and, at the same time, the positive maximum significantly shifted from 567 nm to 600 nm. The most important effect of thermal annealing of sample solutions, however, was the fact that we were able to reproduce the same UV/vis, and CD spectra when different samples were annealed under the same conditions. *b), c)* AFM height and phase images obtained from samples that were prepared from non-annealed solutions of **1** only showed the formation of short nanofibrils with lengths ranging from a few nanometers up to a few hundreds of nanometers, which is in strong contrast to the many micrometers long nanofibrils that were observed after thermal annealing (Figure 3a).

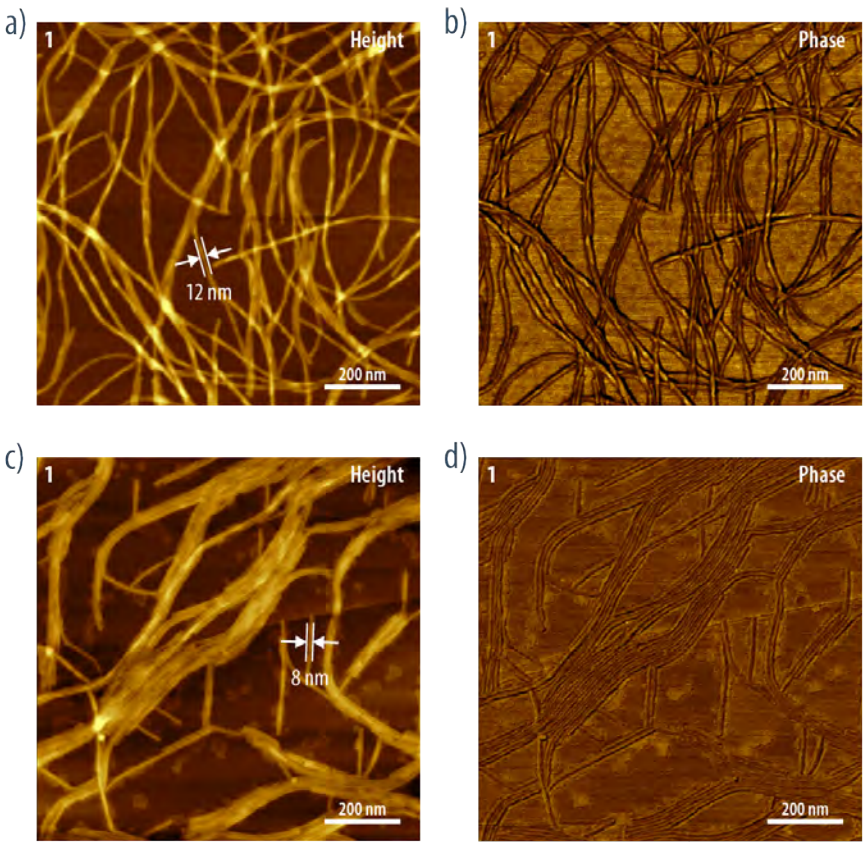

Supplementary Figure S6. *a,b)* Conventional AFM height and phase images of samples of perylene bisimide **1** prepared from thermally annealed and diluted TCE solutions ($c = 5 \cdot 10^{-5}$ mol/L) drop-cast and air-dried on mica substrates proved that nanofibrils with lengths of several micrometers and uniform diameters of 10–12 nm, and heights of 4–5 nm were obtained. Periodic corrugations were occasionally visible in the AFM height image that showed diagonal features in the phase images, indicating the presence of right-handed helical or twisted tapes. *c,d)* On HOPG substrates, the fibrils tended to laterally align, which allowed us to determine nanofibrils diameters of 8.1 ±1.4 nm (from maximum to maximum).

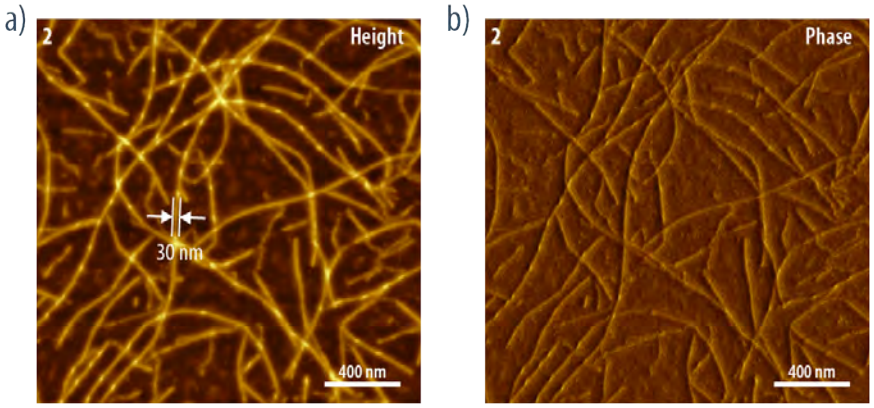

Supplementary Figure S7. *a,b)* Conventional AFM height and phase images of samples of quaterthiophene **2** prepared from thermally annealed and diluted TCE solutions ($c = 5 \cdot 10^{-5}$ mol/L) drop-cast and air-dried on mica substrates revealed the presence of nanofibrils with lengths of several micrometers and mostly uniform apparent diameters; quantitative determination of the latter was obscured by material accumulated along the edges of (and supposedly also underneath) the nanofibrils. Periodic corrugations were occasionally visible in the AFM height image that showed diagonal features in the phase images, indicating the presence of left-handed helical or twisted tapes.

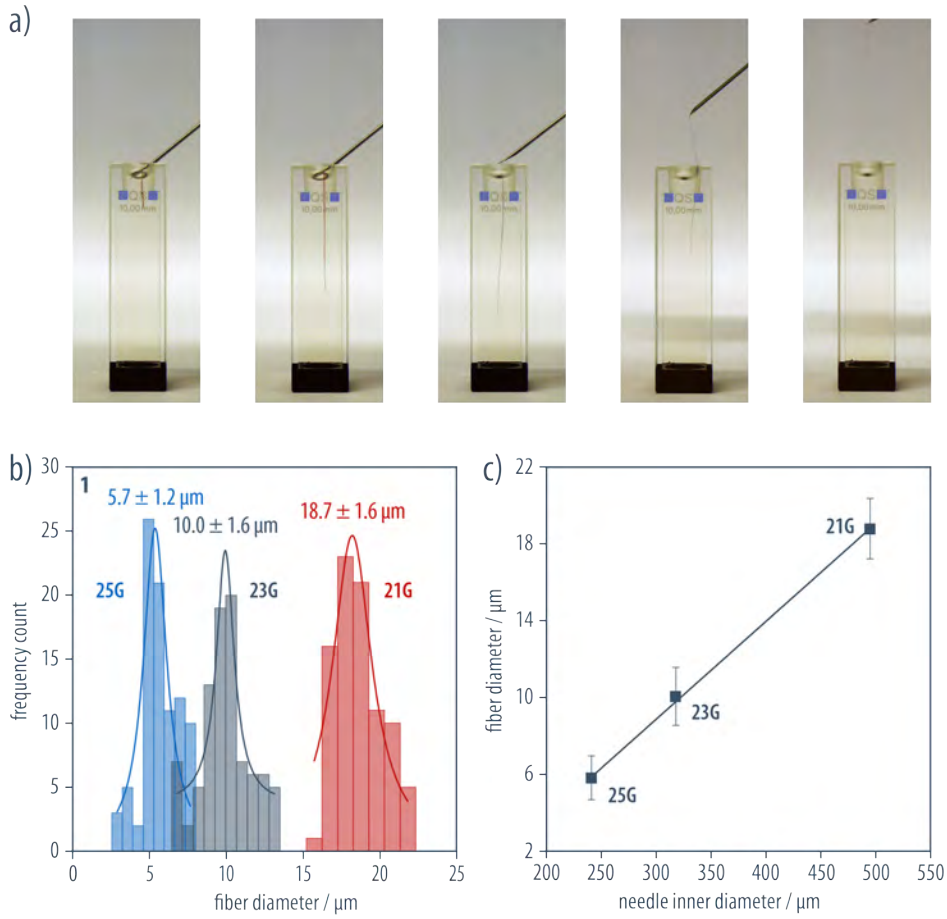

Supplementary Figure S8. *a)* Microfibers were obtained by solution-spinning of nanofibril solutions of **1** (and by analogy **2**; not shown) in TCE ($c = 1 \cdot 10^{-3}$ mol/L) into MeOH. For this purpose, the needle tip of a syringe containing the nanofibril solution was brought into contact with MeOH; gently pushing the syringe stamp then triggered a continuous solvent flow that continued without further pushing. The process was stopped upon removing the needle tip from MeOH once a microfiber of the desired length had been obtained. *b)* The microfiber diameters determined from the scanning electron microscopy (SEM) images (Supplementary Figure S8) could be tuned by varying the needle gauge (21G, red; 23G, grey; 25G, blue). For the histographic analysis, the bin size was determined separately for each histogram according to the Freedman-Diaconis rule,[5] and the distributions were fitted using Gaussian functions. *c)* The thus determined average diameters of the microfibers were well controlled by the needle gauge (G) of 18.7 ± 1.6 µm (21G), 10.0 ± 1.6 µm (23G), and 5.7 ± 1.2 µm (25G) and exhibited a linear relation to the inner diameters of the applied needles.

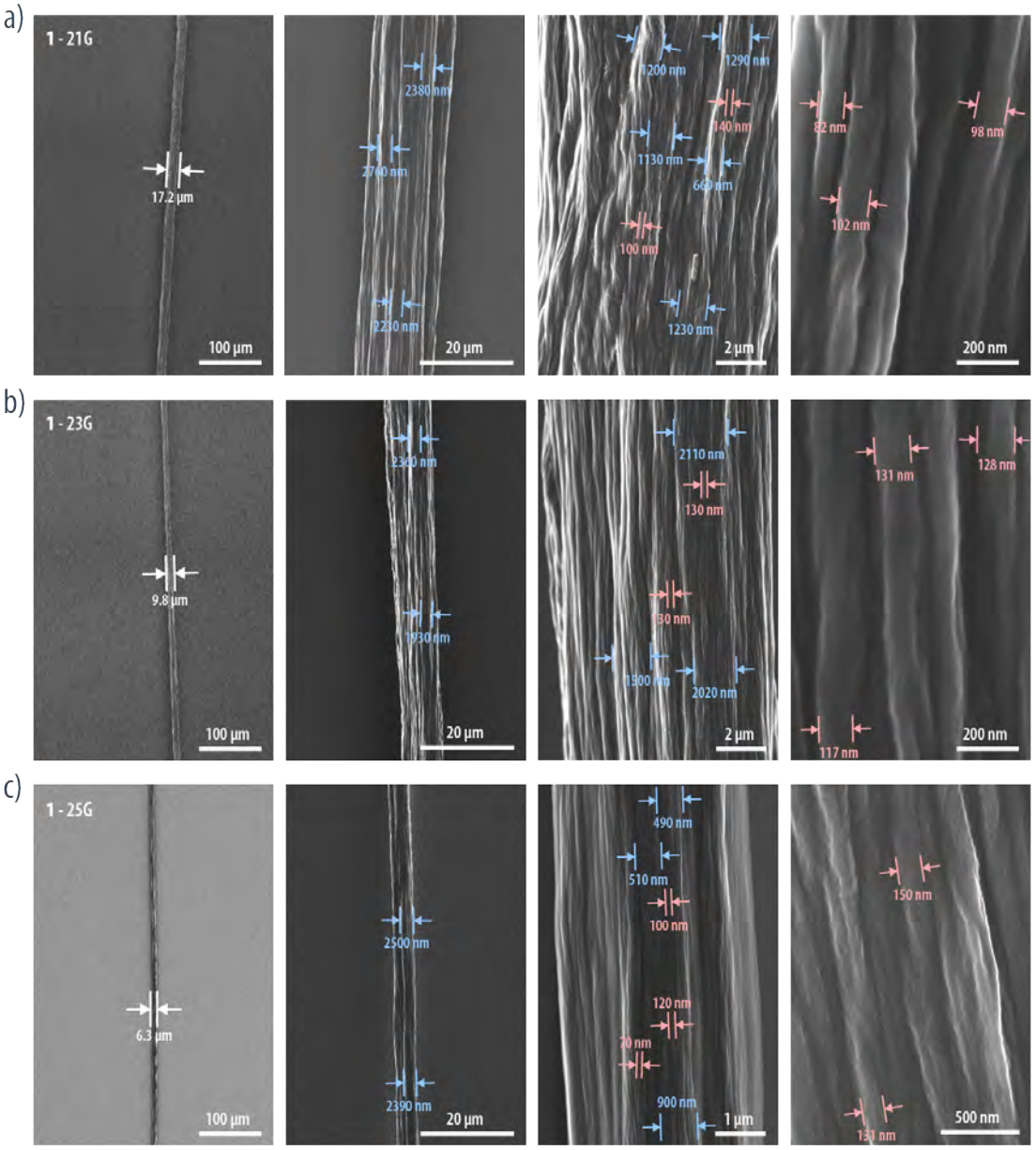

Supplementary Figure S9. Scanning electron microscopy (SEM) images of single microfibers of **1** obtained by solution spinning using *a)* 21G, *b)* 23G, and *c)* 25G needles proved that the diameters of microfibers could be controlled by the applied needle diameter (Supplementary Figure S7). At higher magnifications, it became apparent that these microfibers were hierarchically constituted from highly aligned microfibrils (diameter 500–2700 nm) and smaller protofibrils (diameter 70–150 nm), suggesting that the latter were formed from aligned arrays of the nanofibrils observed in AFM.

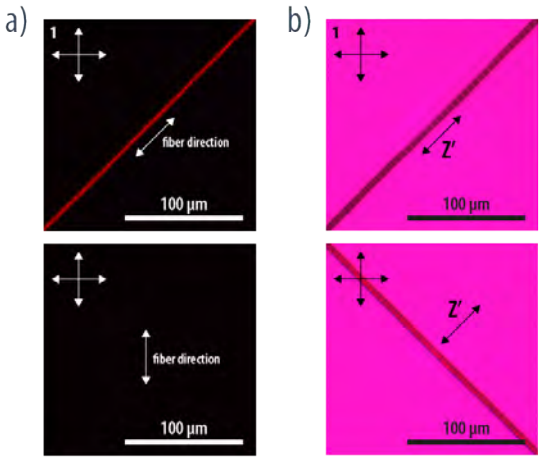

Supplementary Figure S10. *a)* In polarized optical microscopy (POM) under crossed polarizers (orientation indicated by white arrows), maximum birefringence was observed for single microfibers of **1** when the fiber was placed in diagonal position (top), and the sample remained black in extinction position (bottom). These findings are characteristic for a uniaxially oriented system and indicated that the fiber's optical axis was either parallel or perpendicular to the fiber's long axis. *b)* In order to evaluate the direction of the fiber's slow and fast axis, a 530 nm retardation-plate was inserted into the microscope with its slow axis (indicated by the black arrow labeled Z') oriented at 45° to the polarizers. The interference color is expected to be second-order blue if the slow axis of the sample coincides with Z' and first-order yellow when the fast axis of the sample is oriented parallel to Z'. Consistently, the microfibers of became darker in appearance (second-order blue) when oriented parallel to Z' and brighter (first-order yellow) when oriented perpendicular to the direction of the slow axis. Hence, the refractive index was determined to be higher parallel to the long axis of the microfiber, suggesting that the oligopeptide β-strands were oriented perpendicular to the microfiber axis.

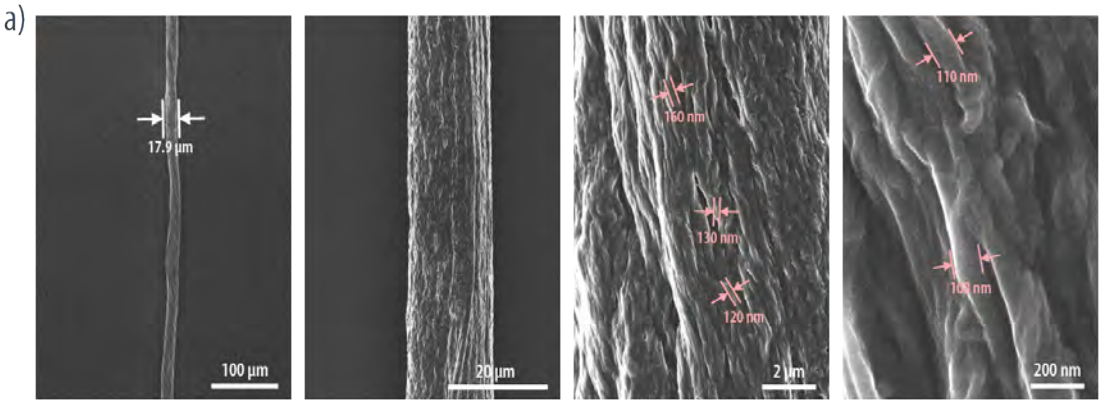

Supplementary Figure S11. Scanning electron microscopy (SEM) images of single microfibers of **2** showed that the constituting microfibrils were well aligned in fiber direction but that the alignment of the smaller protofibrils (110–160 nm) was less perfect as compared to **1**.

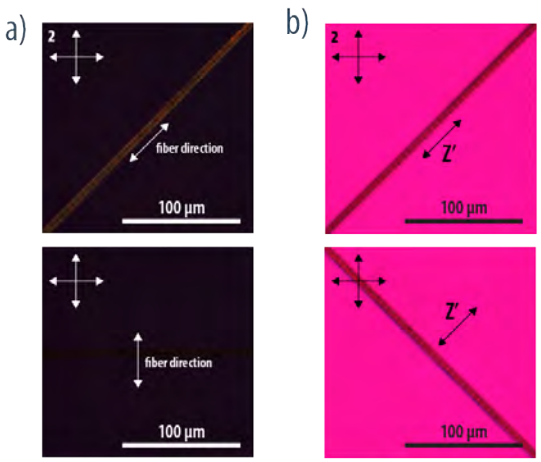

Supplementary Figure S12. *a)* In polarized optical microscopy under crossed polarizers (orientation indicated by white arrows), maximum birefringence was observed for single microfibers of **2** were in diagonal position (top), and the sample remained black in extinction position (bottom). *b)* Upon insertion of a 530 nm retardation-plate (slow axis oriented at 45° to the polarizers, as indicated by the black arrow labeled Z'), the microfibers of became darker in appearance (second-order blue) when oriented parallel to Z' and brighter (first-order yellow) when oriented perpendicular to the direction of the slow axis, consistent with an orientation of the oligopeptide β-strands perpendicular to the microfiber axis.

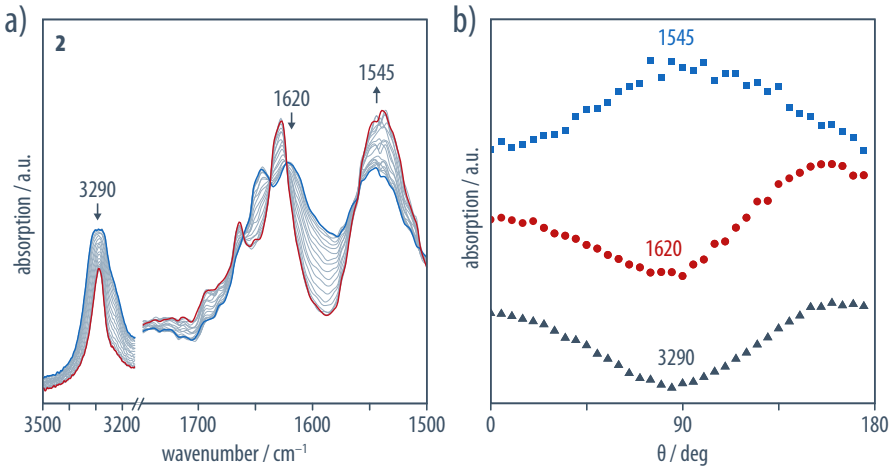

Supplementary Figure S13. *a)* The amide A as well as amide I and II regions of the polarized IR spectra of a single microfiber of **2** (left) with the polarizer perpendicular (90°, red) and parallel (0°, blue) to the microfiber showed an intensification of the absorptions at 3290 and 1620 cm^{-1} in parallel orientation and of the 1545 cm^{-1} band in perpendicular orientation. The grey curves represent the intermediate spectra obtained by increasing the angle between the polarizer and the microfiber from 5° to 85° in steps of 5°. *b)* Consistently, plots of the absorption intensities at 1545 cm^{-1} (blue), 1620 cm^{-1} (red), and 3290 cm^{-1} (grey) *vs*. the angle between polarizer and microfiber (right) showed a maximum at around 90° for the amide II band, and minima at around 90° for both the amide A and amide I bands. These findings implied that the oligopeptide β-stands were perpendicular to the microfiber axis and β-sheet aggregation determined the fast growth direction of the microfibers and their constituent nanofibrils.

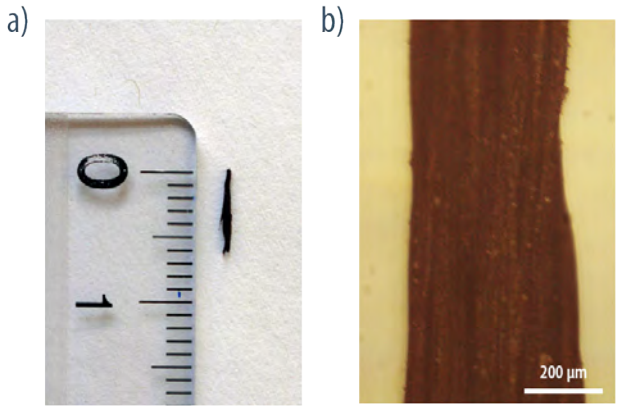

Supplementary Figure S14. *a)* Photograph and *b)* optical micrograph of a bundle of 200 manually aligned microfibers of **1** as investigated by small and wide-angle X-ray (SAXS, WAXS) experiments (Supplementary Figures S14–S16).

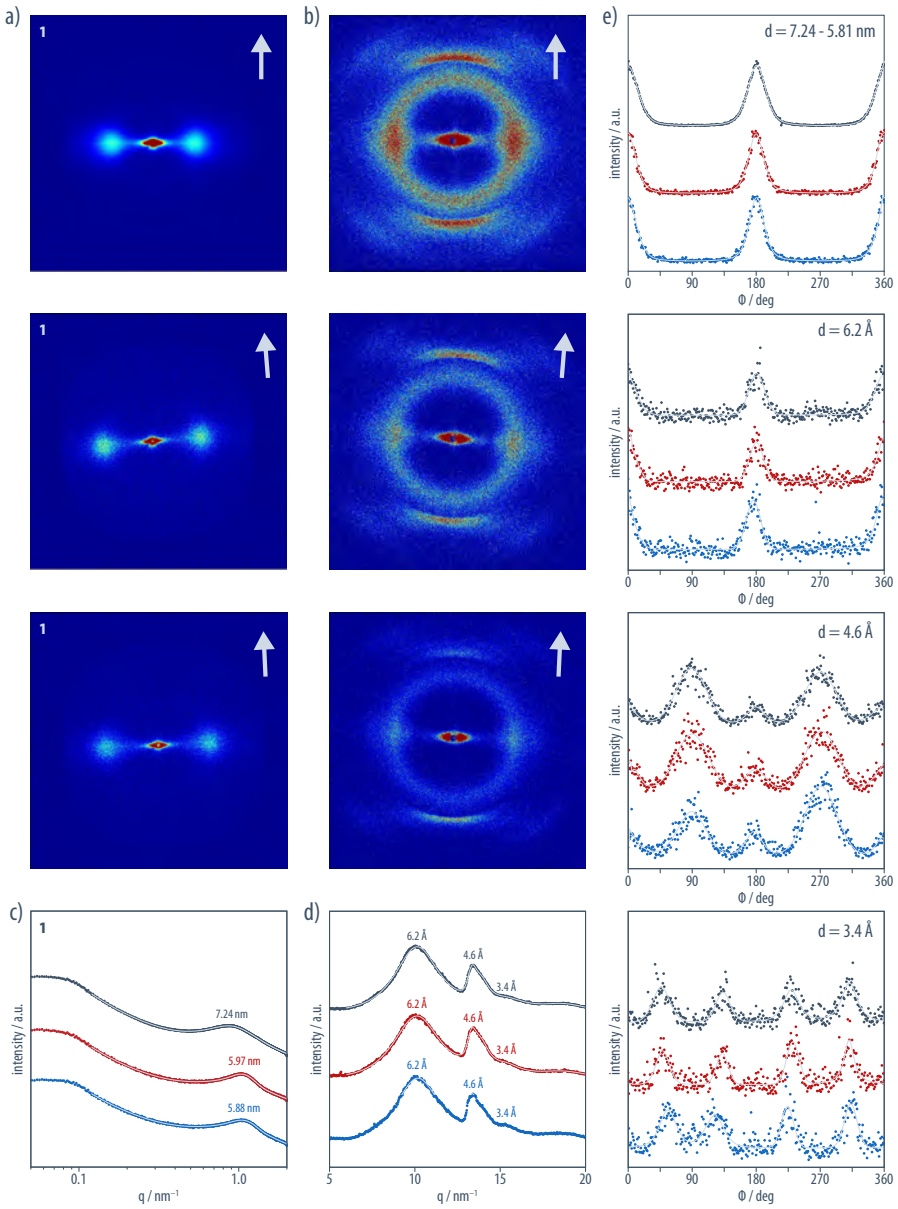

Supplementary Figure S15. *a)* The 2D SAXS and *b)* WAXS patterns of a non-annealed microfiber bundle of perylene bisimide **1** (top), a microfiber bundle after annealing in THF vapor for 7 d (middle), and a microfiber bundle annealed in high vacuum for 48 h (bottom) all showed pronounced anisotropic reflections. Grey arrows indicate the microfiber bundle orientation. *c)* The *q*-vector plots of the SAXS regions of the non-annealed (grey), THF vapor annealed (red), and high vacuum annealed (blue) samples showed single reflections at characteristic distances of $d = 5.88–7.24$ nm ($q = 0.87–1.07$ nm^{-1}) that can be assigned to the tight packing of the nanofibrils into an aligned array within the microfibers. The observed packing distance was significantly smaller than the extended length of the molecules and became smaller upon annealing, indicating that the packing and alignment of the constituting nanofibrils was improved. *d)* The *q*-vector plots of the WAXS regions of the three samples showed three reflections that, in contrast to the SAXS reflection, were not affected by annealing. The reflections at 3.4 Å ($q = 18.7–18.8$ nm^{-1}), 4.6 Å ($q = 13.7–13.8$ nm^{-1}), and 6.2 Å ($q = 10.1–10.2$ nm^{-1}) could be assigned to the π–π stacked conjugated cores, the hydrogen-bonded oligopeptides, and poly(isobutylene) in an average 8_3-helical conformation, respectively. *e)* For all three samples, the azimuthal intensity distributions of the SAXS reflection at $d = 5.88–7.24$ nm showed two maxima at $\phi = 0°$ and 180° indicating that the nanofibrils were oriented parallel to the microfiber axis. The azimuthal intensity distributions of the WAXS reflections at $d = 6.2$ Å exhibited two maxima at $\phi = 0°$ and 180°, suggesting that the terminally attached polymer segment had been sheared along the microfiber axis. The two maxima at $\phi = 90°$ and 270° of the 4.6 Å reflection showed that the oligopeptide β-strands were oriented perpendicular to the microfiber axis, consistent with polarized IR microscopy. The two small maxima at 0° and 180° were assigned to residual intensity from the close reflection of the polymer segment. The 3.4 Å reflection exhibited four maxima at $\phi = 48°$, 180°–ϕ, 180°+ϕ, and 360°–ϕ for the non-annealed sample, $\phi = 49°$, 180°–ϕ, 180°+ϕ, and 360°–ϕ for the solvent-annealed sample, and $\phi = 51°$, 180°–ϕ, 180°+ϕ, and 360°–ϕ for the vacuum-annealed sample, corresponding to conical distributions of the π-conjugated cores with average inclination angles ϕ relative to the microfiber axis.

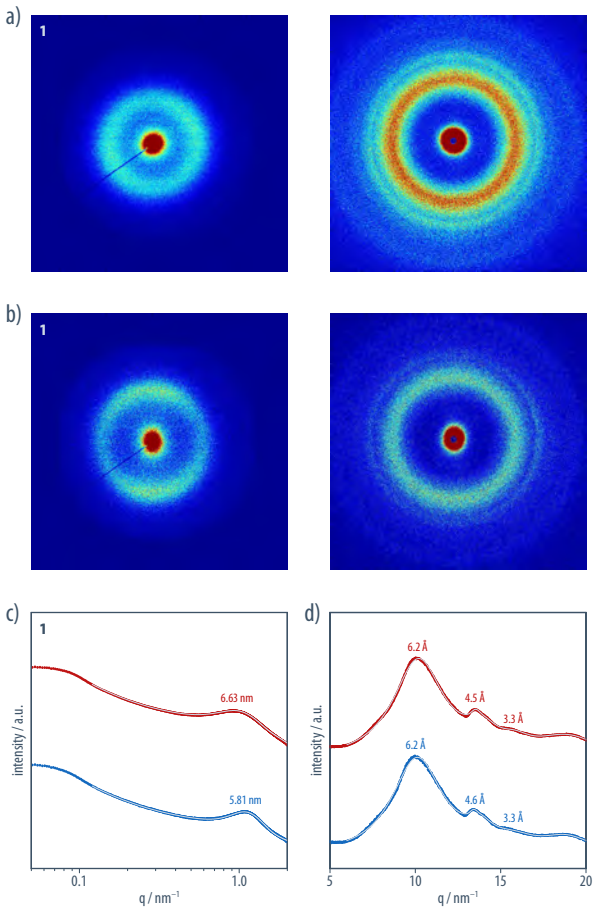

Supplementary Figure S16. The 2D SAXS (left) and WAXS (right) patterns of two control samples obtained by *a)* precipitating a thermally annealed solution of perylene bisimide **1** in TCE into MeOH followed by annealing in high vacuum for 48 h, as well as by *b)* preparing non-aligned coils of solution-spun microfibers both showed isotropic reflections. *c)* The corresponding *q*-vector plots of the precipitate (red), and non-aligned coils (blue) showed reflections at $d = 5.81–6.63$ nm ($q = 0.95–1.08$ nm^{-1}) in the SAXS region, and *d)* at 3.3 Å ($q = 18.9–19.0$ nm^{-1}), 4.5–4.6 Å ($q = 13.7–13.9$ nm^{-1}), and 6.2 Å ($q = 10.1–10.2$ nm^{-1}) in the WAXS region (right) that can be assigned to the packing the nanofibrils in the bulk, the π–π stacking, hydrogen-bonding, and the poly(isobutylene) 8_3-helices.

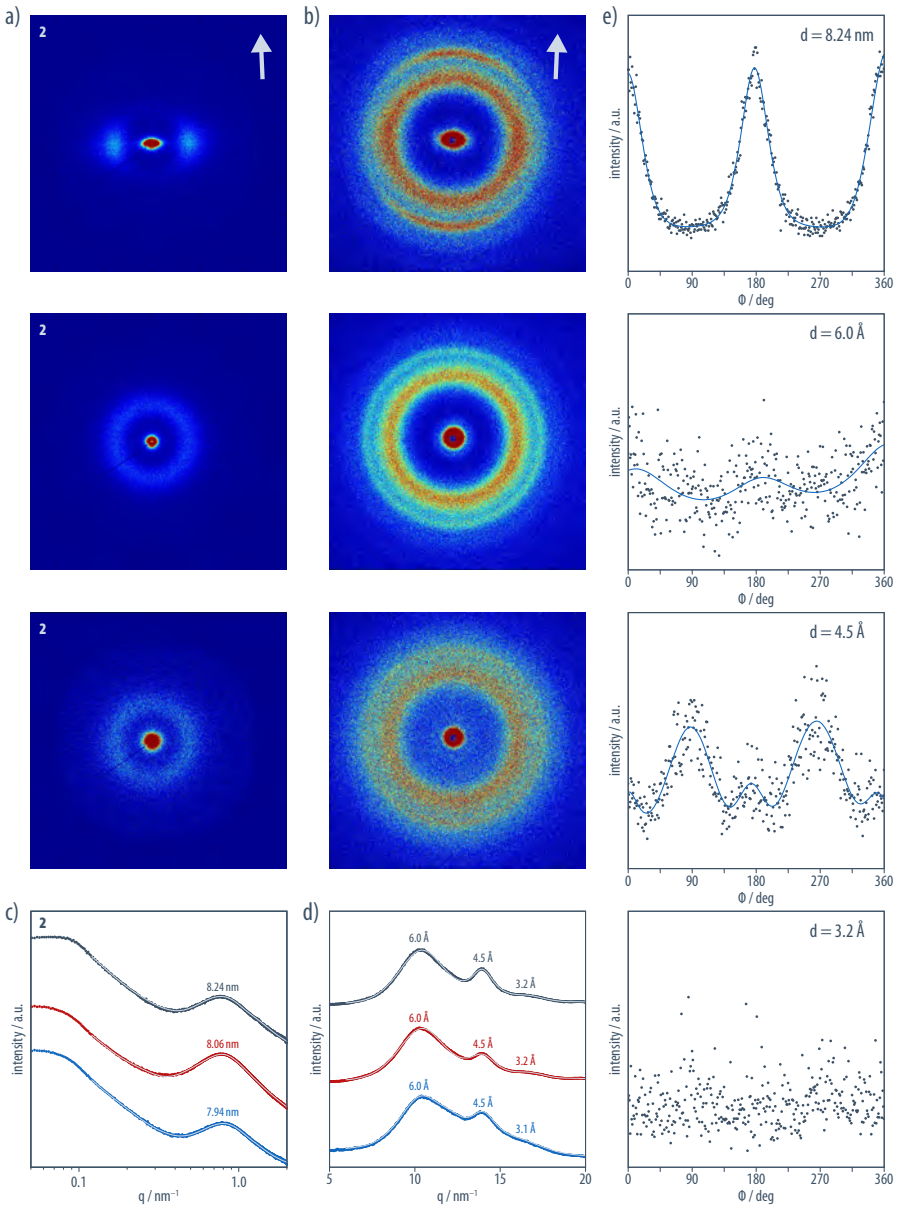

Supplementary Figure S17. *a)* The 2D SAXS and *b)* WAXS patterns of a microfiber bundle of quaterthiophene **2** high vacuum annealed for 48h (top) showed (less pronounced) anisotropic reflections. Grey arrows indicate the microfiber bundle orientation. By contrast, the 2D SAXS and WAXS patterns of control samples obtained by precipitating a thermally annealed solution of quaterthiophene **2** in TCE into MeOH followed by annealing in high vacuum for 48 h (middle), as well as by preparing non-aligned coils of solution-spun microfibers (bottom) showed isotropic reflections. *c)* The *q*-vector plots of the SAXS regions of the aligned fiber bundles (grey), precipitate (red), and non-aligned coils (blue) showed single reflections at characteristic distances of $d = 7.94$–8.24 nm ($q = 0.76$–0.79 nm^{-1}) that can be assigned to the tight packing of the nanofibrils into an aligned array within the microfibers. While the observed distance corresponded well to the diameter of the nanofibrils observed in AFM images, it was significantly smaller than the extended length of the molecules. *d)* The *q*-vector plots of the WAXS regions of the three samples showed three reflections at 3.1–3.2 Å ($q = 19.8$–20.2 nm^{-1}), 4.5 Å ($q = 14.0$ nm^{-1}), and 6.0 Å ($q = 10.4$ nm^{-1}) that were assigned to the π–π stacked conjugated cores, the hydrogen-bonded oligopeptides, and poly(isobutylene) in an average 8_3-helical conformation, respectively. *e)* For microfiber bundles of quaterthiophene **2**, the azimuthal intensity distribution of the SAXS reflection at $d = 8.24$ nm showed two maxima at $\phi = 0°$ and 180° indicating that the nanofibrils were oriented parallel to the microfiber axis. The two azimuthal intensity distribution maxima at $\phi = 0°$ and 180° of the WAXS reflections at $d = 6.0$ Å suggested that the terminally attached polymer segment had been sheared along the microfiber axis. The two maxima at $\phi = 90°$ and 270° of the 4.5 Å reflection showed that the oligopeptide β-strands were oriented perpendicular to the microfiber axis. The two small maxima at 0° and 180° were assigned to residual intensity from the close reflection of the polymer segment. No anisotropic distribution could be determined for the 3.2 Å reflection which, together with the observation that the azimuthal intensity distributions of the SAXS reflections were less well resolved as compared to **1**, indicated a higher degree of disorder and conformational dynamics in the case of the quaterthiophenes **2**.

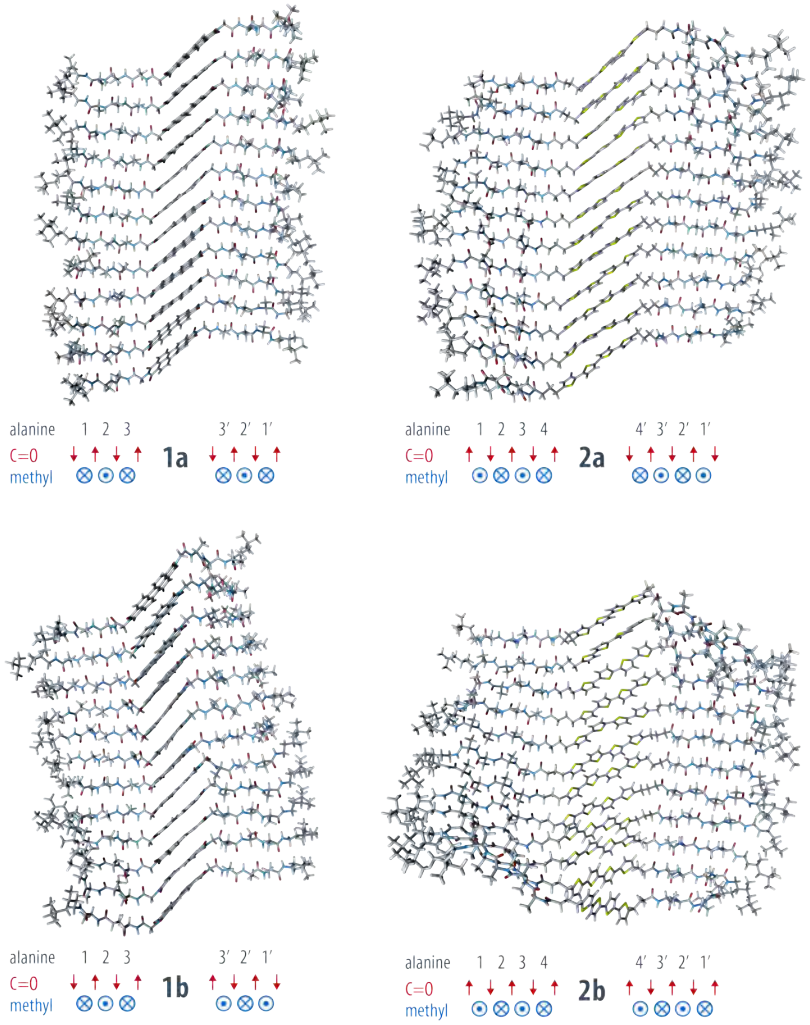

Supplementary Figure S18. Molecular dynamics (MD) simulations were performed at the classical molecular mechanics level for dodecameric aggregates of **1** and **2** (with their polymer termini replaced by simple alkyl groups). The starting geometries were constructed based on regular stacks of conformationally extended monomers with inclination angles relative to the microfiber axis of 90° for both, the oligopeptide and the π-conjugated segments, and considering two possible molecular conformations and supramolecular arrangements. Thus, the two inner-most oligopeptide carbonyl groups (indicated by the red arrows) in models **1a** and **2a** were oriented in opposite directions, so as to minimize the global dipole-moment of the assembly. By contrast, they pointed into the same direction in models **1b** and **2b**, which results in a more balanced steric load on the two faces of the β-sheet tapes for uneven numbers of L-alanine methyl side groups, as is the case for **1** (blue ⊗ and ⊙ indicating methyl groups pointing into and out of the plane of projection). The displayed structures **1a,b** and **2a,b** were taken from a 15 ns MD simulation after 25 ns equilibration. A complete listing of the calculated numerical values for hydrogen-bonding and π–π-stacking distances, inclination angles of the oligopeptide- and π–conjugated segment with respect to the fiber axis, as well as rotational displacement angles between the chromophores is provided in Table S5. Whereas the structures of **1a** and **2a** were in good agreement with the experimental findings, **1b** and **2b** could be discarded. Thus, **1b** did not exhibit a global handedness but instead featured a characteristic transition from a left- to a right-handed twist within the same fiber. For the first 10 ns of the simulation, **2b** shared the same characteristics as **1b** but during the following 30 ns the assembly featured a left-handed helical twist. It may be assumed that the combination of a more flexible linker and reduced π–π-stacking interactions enabled this transition.

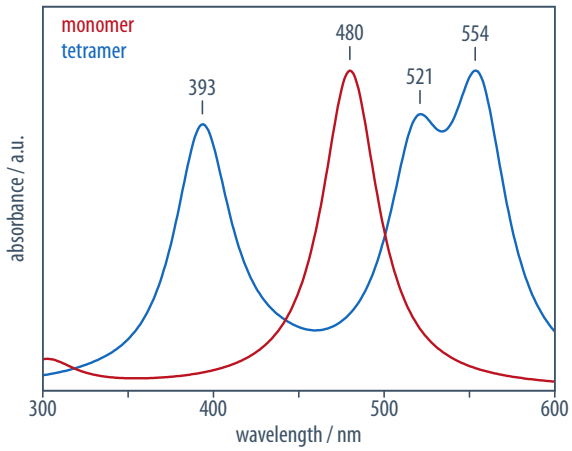

Supplementary Figure S19. The UV/vis spectra of a single perylene bisimide core (red) and a stack of four molecules of **1** (blue) based on averaged geometries obtained by the MD simulations were obtained from DFT computations using the ωB97X-D/def2-SVP functional to account for weak long-range interactions. The disappearance of the monomer peak combined with the appearance of one hypsochromically shifted and two bathochromically shifted absorption bands in the aggregates are in excellent qualitative and quantitative agreement with our experimental findings. Note that the long-range corrected functional ωB97X-D was superior to standard global hybrid functionals (e.g., B3LYP) that introduce spurious charge-transfer character into the UV/vis spectrum of perylene bisimide.[6] The ~0.3 eV (~60 nm) blue shift observed between the computational and experimental spectrum is in the typical difference range between vertical excitations and 0-0 transition energies for polycyclic hydrocarbons.[7]

2. Supplementary Tables S1–S5

Table S1. Scattering wave vectors q, distances d, and correlation lengths ξ of the four SAXS and WAXS reflections of the perylene bisimide samples, assigned to the nanofibril diameter, the poly(isobutylene) (PIB) packing, the oligopeptide β-sheet aggregation, and the π–π stacking of the perylene bisimide cores.

sample	q_{fibril} / nm^{-1} d_{fibril} / nm ξ_{fibril} / nm	q_{PIB} / nm^{-1} d_{PIB} / Å ξ_{PIB} / Å	q_{β} / nm^{-1} d_{β} / Å ξ_{β} / Å	$q_{\pi-\pi}$ / nm^{-1} $d_{\pi-\pi}$ / Å $\xi_{\pi-\pi}$ / Å
non-annealed aligned fiber bundle	0.87 7.24 9.79	10.1 6.2 20	13.7 4.6 65	18.8 3.4 17
THF-vapor annealed aligned fiber bundle	1.05 5.97 17.4	10.1 6.2 19	13.7 4.6 58	18.7 3.4 15
vacuum-annealed aligned fiber bundle	1.07 5.88 16.9	10.2 6.2 20	13.8 4.6 61	18.7 3.4 16
vacuum-annealed precipitated material	0.95 6.63 11.8	10.2 6.2 17	13.9 4.5 29	19.0 3.3 15
vacuum-annealed non-aligned fibers	1.08 5.81 13.3	10.1 6.2 17	13.7 4.6 35	18.9 3.3 17

Table S2. Azimuthal peak maxima (ϕ) and order parameters (S) of the four peaks in the SAXS and WAXS patterns for the three perylene bisimide-based fibers.

sample	ϕ_{fibril} S_{fibril}	ϕ_{PIB} S_{PIB}	ϕ_{β} S_{β}	$\phi_{\pi-\pi}$ $S_{\pi-\pi}$
non-annealed aligned fiber bundle	0°, 180° 0.72	0°, 180° 0.87	90°, 270° -0.29	48°, 132°, 228°, 312° 0.86
THF-vapor annealed aligned fiber bundle	0°, 180° 0.77	0°, 180° 0.86	90°, 270° -0.27	49°, 131°, 229°, 311° 0.92
vacuum-annealed aligned fiber bundle	0°, 180° 0.76	0°, 180° 0.89	90°, 270° -0.29	51°, 129°, 231°, 309° 0.87

Table S3. Scattering wave vectors (q), distances (d) and correlation lengths (ξ) of the four peaks in the SAXS and WAXS patterns for the three quaterthiophene-based samples.

sample	q_{fibril} / nm^{-1} d_{fibril} / nm ξ_{fibril} / nm	q_{PIB} / nm^{-1} d_{PIB} / Å ξ_{PIB} / Å	q_{β} / nm^{-1} d_{β} / Å ξ_{β} / Å	$q_{\pi-\pi}$ / nm^{-1} $d_{\pi-\pi}$ / Å $\xi_{\pi-\pi}$ / Å
vacuum-annealed aligned fiber bundle	0.76 8.24 14.9	10.4 6.0 20	14.0 4.5 36	19.8 3.2 16
vacuum-annealed precipitated material	0.78 8.06 12.4	10.4 6.0 19	14.0 4.5 28	19.7 3.2 16
vacuum-annealed non-aligned fibers	0.79 7.94 10.2	10.4 6.0 17	14.0 4.5 31	20.2 3.1 14

Table S4. Azimuthal peak maxima (ϕ) and order parameters (S) of the four peaks in the SAXS and WAXS patterns for the quaterthiophene-based fiber.

sample	ϕ_{fibril} / deg S_{fibril}	ϕ_{PIB} / deg S_{PIB}	ϕ_{β} / deg S_{β}
vacuum annealed fiber bundle	0, 180 0.58	0, 180 0.22	90, 270 -0.16

Table S5. Distances (d), inclination angles (ϕ) relative to the fiber axis, and rotational displacement angle (α) for the models **1a,b** and **2a,b** obtained as averages over a 15 ns MD simulation after 25 ns equilibration.

model	d_{β} / Å	$d_{\pi-\pi}$ / Å	$\phi_{\pi-\pi}$	α_{twist}	ϕ_{β}
1a	4.7 ± 0.1	3.5 ± 0.1	48 ± 2°	-4 ± 4°	89 ± 2°
1b	4.8 ± 0.2	3.6 ± 0.2°	49 ± 3°	NA	90 ± 3°
2a	4.8 ± 0.1	3.9 ± 0.2	55 ± 4°	-5 ± 4°	90 ± 3°
2b	4.8 ± 0.1	4.2 ± 0.2	62 ± 5°	-8 ± 6°	89 ± 3°

3. Experimental Part

3.1. Instrumentation and Methods

NMR Spectroscopy. ^{1}H NMR spectroscopy was carried out on a Bruker Avance 400 spectrometer operating at 400.23 MHz. Deuterated solvents were purchased from Cambridge Isotope Laboratories. Chemical shifts (δ) were reported in ppm, with the solvent resonance as the internal standard relative to 1,1,2,2-tetrachloroethane-d_2 (δ 6.0) for ^{1}H. Data are reported as follows: s = singlet, d = doublet, t = triplet, q = quartet, m = multiplet). Coupling constants J are reported in Hz. The coupling patterns and coupling constants were evaluated with Mestrenova NMR data processing.

Mass Spectrometry. Mass Spectra were recorded at the mass spectrometry service at EPFL on either a Shimadzu Biotech AXIMA Performance device for MALDI-TOF.

IR Spectroscopy and Polarized IR Microscopy. Solution-phase IR spectra ($1 \cdot 10^{-3}$ M in TCE) were recorded on a Jasco FTIR 6300 spectrometer using a solution phase cell with KBr windows and a path length of 500 μm. Polarized IR microscopy on single microfibers was carried out on a Jasco IRT-5000 FTIR microscope coupled to a Jasco FTIR 4100. The microscope was equipped with a wire-grid-infrared polarizer whose rotation was software-controlled from 0° to 180° in steps of 1°. The sample was put onto a KBr plate and measured in transmission. The resolution was set to 4 cm^{-1} for both, IR spectroscopy and polarized IR microscopy.

Vibrational Circular Dichroism Spectroscopy. Solution phase VCD spectra ($1 \cdot 10^{-3}$ M in TCE) were recorded on a dual-modulator BioTools ChiralIR-2X spectrometer using a cell made of BaF_2 windows and a path length of 100 μm. While recording the spectra the cell was rotated in order to avoid any anisotropy effects. The spectra were obtained by taking the average of five packages, each package consisting of 1000 scans, and applying a raised cosine apodization. The resolution was 4 cm^{-1}.

UV/vis and CD Spectroscopy. Solution phase UV/vis spectra ($1 \cdot 10^{-4}$ M in TCE) were recorded on a Jasco V-670 spectrometer using a Hellma quartz cuvette with 1 mm path length. Solution phase CD spectra were recorded on a Jasco J-815 spectrometer using a Hellma quartz cuvette with 1 mm path length. Both, the UV/vis and the CD spectrometer were equipped with a Jasco ETCR-762 temperature controller connected to a Jasco MCB-100 mini circulation bath. The resolution was set to 1 nm for both, UV/vis and CD specroscopy.

Polarized Optical Microscopy. Polarized optical microscopy on single microfibers was carried out on a Olympus BX-60 microscope.

Static Light Scattering. Static light scattering measurements were performed using a LS Instruments machine equipped with He-Ne laser emitting a polarized light beam of wavelength of 632.8 nm. The cross-correlated static light scattering measurements of a solution of **2** ($1 \cdot 10^{-4}$ M in TCE) were performed at different scattering angles ranging from 40° to 140° at steps of 10° by averaging 3 runs of 600 seconds each. The range of scattering vector, q, covered was 0.01 $nm^{-1} < q < 0.028 nm^{-1}$ with $q = 4\pi n/\lambda \sin(\theta/2)$, where λ, n and θ are the light source wavelength, the solvent refractive index of TCE, and the angle between the detector and the incident beam respectively. The raw intensity values were corrected for background from the solvent (TCE).

Scanning Electron Microscopy. Microfibers of **1** and **2** prepared by solution-spinning were placed onto SiO_2 substrates that had been pretreated with ethanol and ultrapure water. All samples for statistic evaluation were coated with 12 nm of carbon. A Philips FEI XLF30-FEG SEM operating at 3-5 keV was used to image the samples. Ultra-high resolution SEM were obtained on a Phillips FEI XLF30-SFEG SEM operating at 3 keV, using samples coated with 4 nm of OsO_4.

Molecular Dynamics Simulations and Density Functional Theory Computations. The MD simulations were performed with the AMBER 11 program.[8,9] The oligopeptide residues were described by the FF99SB AMBER force field[10] and the remaining parts by standard GAFF parameters[11] in combination with AM1-BCC[12] atomic charges. The initial chloroform solvation box had a minimal distance of 10 Å from the solute. Constant temperature (300 K) was maintained with a Langevin thermostat[13] (collision frequency of 2 ps^{-1}), and the pressure (1 bar) was regulated with a Berendsen barostat[14] (relaxation time of 1 ps and the default compressibility). The electrostatic interactions were evaluated with a particle mesh-Ewald summation[15] (real space of 8 Å), and all bonds towards hydrogens were fixed with the SHAKE algorithm[16] and an integration step of 2 fs. In general, the geometrical analysis was restricted to extracting information from the four central monomers within a dodecamer. To decrease fluctuations, atom positions were averaged when necessary. Simulations were performed for 40 ns. The data from the last 15 ns of simulation (corresponding to 6000 snapshots) were considered, after 25 ns of equilibration time. The angle between the fiber axis and the peptide axis was averaged over eight similar values (on the „left“ and „right“, each time defining the fiber axis either with the first carbonyl carbon or the first amide nitrogen starting from the π-conjugated core corresponding to one of the two central monomers). Similarly, the angle between the fiber axis and the π-conjugated core was averaged over four values related to the two central monomers. The twisting angle was averaged over the three consecutive dihedrals connecting the central four monomers. Finally, the repeat unit was defined by the average of two distances between the first carbonyl carbon atoms on the left and right of the π-conjugated core. The π–π stacking distance was calculated according to $r \cdot sin(a)$, with r being the averaged repeat unit and α the averaged fiber-π angle. The theoretical UV/vis spectra are based on a single perylene bisimide core as well as a stack of four perylene bisimide molecules that were extracted as averages over 400 snapshots (1 ns) of **1a**. The linker was saturated with a hydrogen atom at a distance of 1.07 Å. The absorption spectra (Supplementary Figure S18) were obtained from DFT computations at the ωB97X-D[17]/def2-SVP[18] level using Gaussian09.[19]

3.2. Analytical Data for Compounds 1 and 2

1: ^{1}H NMR (400 MHz, 0.6 mL $C_2D_2Cl_4$, + 10 μL TFA-d1) δ 8.78 - 8.45 (m, 8H, aromatic *H*), 7.54 (s, 1H, N*H*), 7.43 (s, 2H, N*H*), 6.75 (s, 1H, N*H*), 5.22 - 4.37 (m, 10H, 6x C*H*CH_3, NHCOCH_2NCO), 3.23 (s, 4H, PIB-CH_2NHCO), 1.94 - 0.82 (m, 393H, polymer *H*). MS (MALDI): calcd. mass for $C_{140}H_{234}N_{10}O_{12}Na$ ([M(n_1 = 9, n_2 = 10)+Na]$^+$) 2272.4050; found 2272.1378.

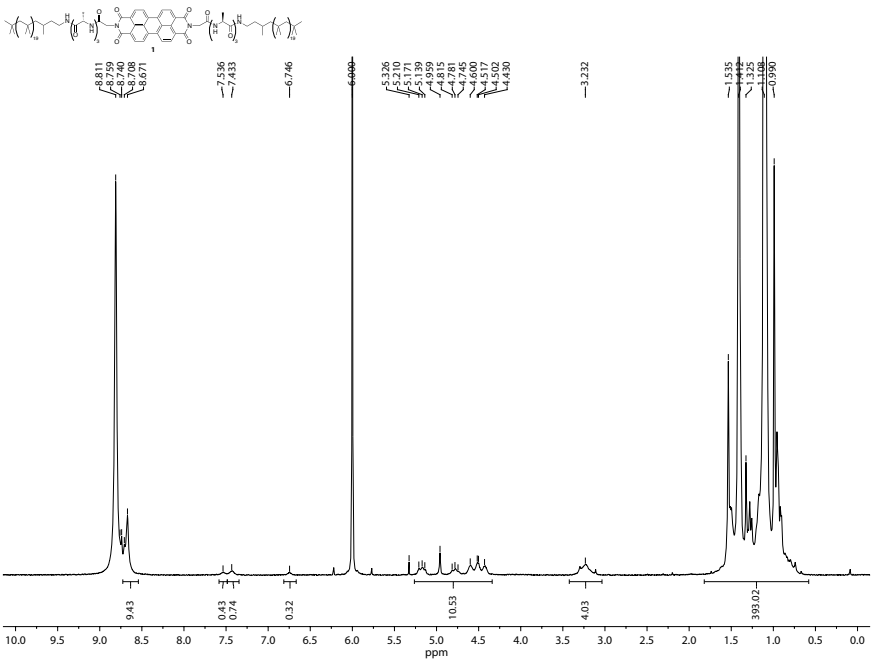

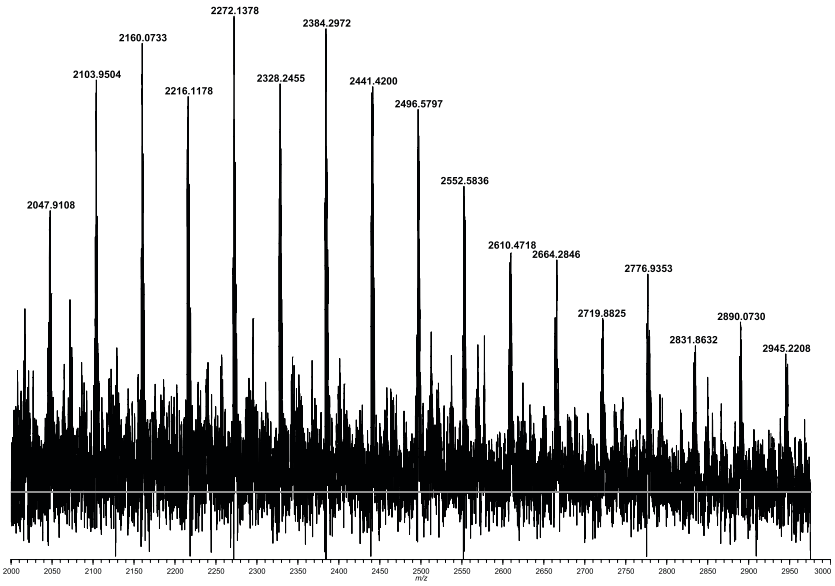

2: ^{1}H NMR (400 MHz, $C_2D_2Cl_4$, 383 K) δ 7.15 - 7.04 (m, 6H, aromatic *H*), 6.79 - 6.77 (m, 2H, aromatic *H*), 6.58 (s, 4H, N*H*), 6.41 (s, 2H), 5.98 (s, 2H, N*H*), 5.85 (s, 2H, N*H*), 4.45 - 4.37 (m, 8H, C*H*CH_3), 3.35 - 3.26 (m, 4H, PIB-CH_2NHCO), 2.98 - 2.90 (m, 4H, NCOCH_2CH_2CH_2-T), 2.42 - 2.32 (m, 4H, NCOCH_2CH_2CH_2-T), 2.17 - 2.07 (m, 4H, NCOCH_2CH_2CH_2-T), 1.60 - 0.92 (m, 660H, polymer *H*) ppm. MS (MALDI): calcd. mass for $C_{182}H_{332}N_{10}O_{10}S_4Na$ ([M(n_1 = 13, n_2 = 14)+Na]$^+$) 2858.3335; found 2858.3956.

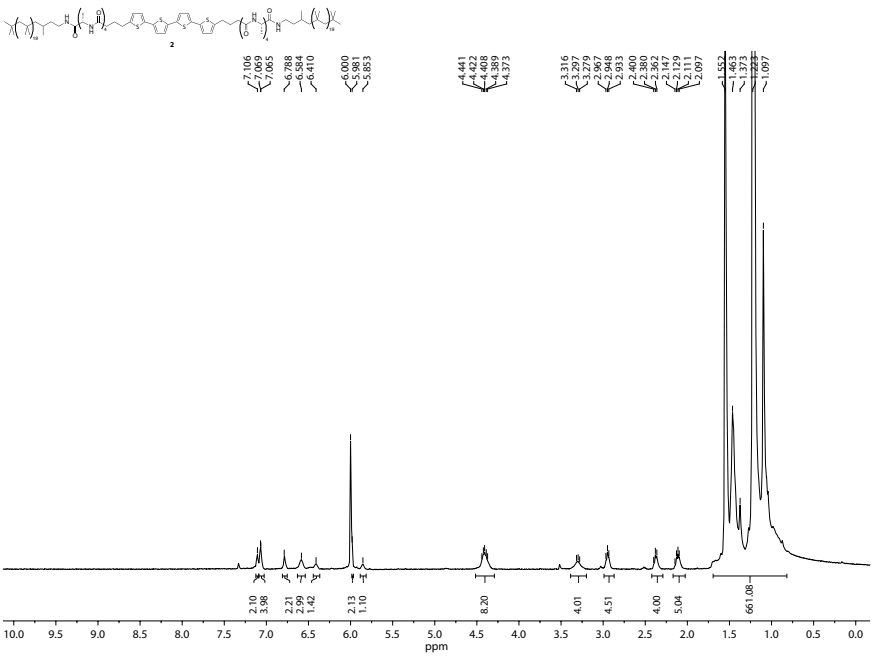

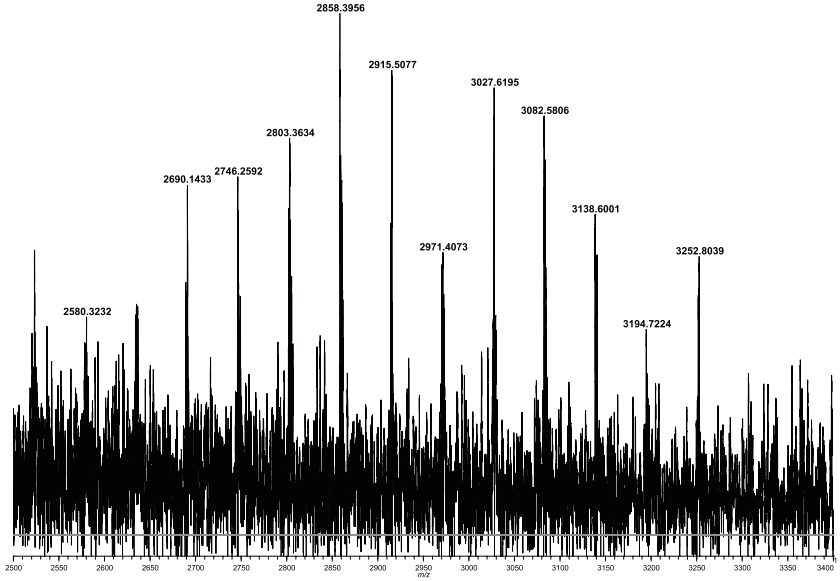

4. References

1. Chen, Z.; Stepanenko, V.; Dehm, V.; Prins, P.; Siebbeles, L. D. A.; Seibt, J.; Marquetand, P.; Engel, V.; Würthner, F. Photoluminescence and Conductivity of Self-Assembled π–π Stacks of Perylene Bisimide Dyes *Chem. Eur. J.* **2007**, *13*, 436–449.
2. Thalacker, C.; Würthner, F. Chiral Perylene Bisimide–Melamine Assemblies: Hydrogen Bond-Directed Growth of Helically Stacked Dyes with Chiroptical Properties *Adv. Funct. Mater.* **2002**, *12*, 209–218.
3. Dehm, V.; Chen, Z.; Baumeister, U.; Prins, P.; Siebbeles, L. D. A.; Würthner, F. Helical Growth of Semiconducting Columnar Dye Assemblies Based on Chiral Perylene Bisimides *Org. Lett.* **2007**, *9*, 1085–1088.
4. Kawano, S.-I.; Fujita, N.; Shinkai, S. Quater-, Quinque-, and Sexithiophene Organogelators: Unique Thermochromism and Heating-Free Sol-Gel Phase Transition *Chem. Eur. J.* **2005**, *11*, 4735–4742.
5. Freedman, D.; Diaconis, P. On the Histogram as a Density Estimator: L2 Theory *Z. Wahrscheinlichkeit.* **1981**, *57*, 453–476.
6. Zhao, H.-M.; Pfister, J.; Settels, V.; Renz, M.; Kaupp, M.; Dehm, V. C.; Würthner, F.; Fink, R. F.; Engels, B. Understanding Ground- and Excited-State Properties of Perylene Tetracarboxylic Acid Bisimide Crystals by Means of Quantum Chemical Computations *J. Am. Chem. Soc.* **2009**, *131*, 15660–15668.
7. Dierksen, M.; Grimme, S. Density Functional Calculations of the Vibronic Structure of Electronic Absorption Spectra *J. Chem. Phys.* **2004**, *120*, 3544–3554.
8. Pearlman, D. A.; Case, D. A.; Caldwell, J. W.; Ross, W. S.; Cheatham Iii, T. E.; DeBolt, S.; Ferguson, D.; Seibel, G.; Kollman, P. AMBER, A Package of Computer Programs for Applying Molecular Mechanics, Normal Mode Analysis, Molecular Dynamics and Free Energy Calculations to Simulate the Structural and Energetic Properties of Molecules *Comput. Phys. Commun.* **1995**, *91*, 1–41.
9. Case, D. A.; Cheatham, T. E.; Darden, T.; Gohlke, H.; Luo, R.; Merz, K. M.; Onufriev, A.; Simmerling, C.; Wang, B.; Woods, R. J. The Amber Biomolecular Simulation Programs *J. Comput. Chem.* **2005**, *26*, 1668–1688.
10. Hornak, V.; Abel, R.; Okur, A.; Strockbine, B.; Roitberg, A.; Simmerling, C. Comparison of Multiple Amber Force Fields and Development of Improved Protein Backbone Parameters *Proteins* **2006**, *65*, 712–725.
11. Wang, J.; Wolf, R. M.; Caldwell, J. W.; Kollman, P. A.; Case, D. A. Development and Testing of a General Amber Force Field *J. Comput. Chem.* **2004**, *25*, 1157–1174.
12. Jakalian, A.; Jack, D. B.; Bayly, C. I. Fast, Efficient Generation of High-Quality Atomic Charges. AM1-BCC Model: II. Parameterization and Validation *J. Comput. Chem.* **2002**, *23*, 1623–1641.
13. Loncharich, R. J.; Brooks, B. R.; Pastor, R. W. Langevin Dynamics of Peptides: The Frictional Dependence of Isomerization Rates of N-aAetylalanyl-N′-Methylamide *Biopolymers* **1992**, *32*, 523–535.
14. Berendsen, H. J. C.; Postma, J. P. M.; van Gunsteren, W. F.; DiNola, A.; Haak, J. R. Molecular Dynamics with Cupling to an External Bath *J. Chem. Phys.* **1984**, *81*, 3684–3690.
15. Darden, T.; York, D.; Pedersen, L. Particle mesh Ewald: An N [Center-Dot] log(N) Method for Ewald Sums in Large Systems *J. Chem. Phys.* **1993**, *98*, 10089–10092.
16. Ryckaert, J.-P.; Ciccotti, G.; Berendsen, H. J. C. Numerical Integration of the Cartesian Equations of Motion of a System with Constraints: Molecular Dynamics of n-Alkanes *J. Comp. Phys.* **1977**, *23*, 327–341.
17. Chai, J.-D.; Head-Gordon, M. Long-Range Corrected Hybrid Density Functionals with Damped Atom-Atom Dispersion Corrections *Phys. Chem. Chem. Phys.* **2008**, *10*, 6615–6620.
18. Weigend, F.; Ahlrichs, R. Balanced Basis Sets of SplitValence, Triple Zeta Valence and Quadruple Zeta Valence Quality for H to Rn: Design and Assessment of Accuracy *Phys. Chem. Chem. Phys.* **2005**, *7*, 3297–3305.
19. Gaussian 09, Revision A.1, Frisch, M. J.; Trucks, G. W.; Schlegel, H. B.; Scuseria, G. E.; Robb, M. A.; Cheeseman, J. R.; Scalmani, G.; Barone, V.; Mennucci, B.; Petersson, G. A. *et al*. Gaussian Inc.: Wallingford CT, **2009**.